Oil & Natural Gas Technology

DOE Award No.: DE-FE0001243

Topical Report

PORE SCALE ANALYSIS OF OIL SHALE/SANDS PYROLYSIS

Submitted by:
University of Utah
Institute for Clean and Secure Energy
155 South 1452 East, Room 380
Salt Lake City, Utah 84112

Prepared for:
United States Department of Energy
National Energy Technology Laboratory

March, 2011

Office of Fossil Energy

Pore Scale Analysis of Oil Shale/Sands Pyrolysis

Topical Report

Reporting Period: October 1, 2009 through December 31, 2010

Principal Authors: Chen-Luh Lin, and Jan D. Miller

Report Issued: February 2011

DOE Award No.: DE-FE0001243

University of Utah
Institute for Clean and Secure Energy
155 South 1452 East, Room 380
Salt Lake City, Utah 84112

Acknowledgement

This report was prepared as an account of work sponsored by an agency of the United States Government. Neither the United States Government nor any agency thereof, nor any of their employees, makes any warranty, express or implied, or assumes any legal liability or responsibility for the accuracy, completeness, or usefulness of any information, apparatus, product, or process disclosed, or represents that its use would not infringe privately owned rights. Reference herein to any specific commercial product, process, or service by trade name, trademark, manufacturer, or otherwise does not necessarily constitute or imply its endorsement, recommendation, or favoring by the United States Government or any agency thereof. The views and opinions of authors expressed herein do not necessarily state or reflect those of the United States Government or any agency thereof.

ABSTRACT

There are important questions concerning the quality and volume of pore space that is created when oil shale is pyrolyzed for the purpose of producing shale oil. In this report, 1.9 cm diameter cores of Mahogany oil shale were pyrolyzed at different temperatures and heating rates. Detailed 3D imaging of core samples was done using multiscale X-ray computed tomography (CT) before and after pyrolysis to establish the pore structure. The pore structure of the unreacted material was not clear. Selected images of a core pyrolyzed at 400^{o}C were obtained at voxel resolutions from 39 microns (μm) to 60 nanometers (nm). Some of the pore space created during pyrolysis was clearly visible at these resolutions and it was possible to distinguish between the reaction products and the host shale rock. The pore structure deduced from the images was used in Lattice Boltzmann simulations to calculate the permeability in the pore space. The permeabilities of the pyrolyzed samples of the silicate-rich zone were on the order of millidarcies, while the permeabilities of the kerogen-rich zone after pyrolysis were very anisotropic and about four orders of magnitude higher.

EXECUTIVE SUMMARY

The most significant domestic oil shale deposits are in the Green River Formation of Colorado, Utah, and Wyoming, with an estimated resource size of 1.5-1.8 trillion barrels. These oil shale resources will be used primarily for producing transportation fuels. In a carbon-constrained world, transportation fuel production from these resources will require an understanding of processes that occur over a wide range of length and time scales from the structure of kerogen and how its binds to an inorganic matrix to the fluid flow resulting from in situ processing of an oil shale interval that covers hundreds of acres. In this regard, parameters which are important for the analysis of the in-situ pyrolysis processing of oil shale include:

1. Kerogen conversion to oil, gas and coke
2. Nature of the pore space before and after pyrolysis
3. Porous media characteristics after pyrolysis
4. Permeabilities, and
5. Relative permeabilities.

This report describes efforts to address the very challenging characterization problems of items 2 to 5.

To improve our understanding of transport phenomena involved in the in-situ pyrolysis processing of oil shale, the pore scale analysis of oil shale during pyrolysis at different temperatures is critical. The pore space of the oil shale samples before and after pyrolysis was characterized and digitized using multi-scale, non-invasive, non-destructive 3D imaging by X-ray micro/nano CT (XMT/XNT). For example, using a combination of XMT/XNT and specialized software, the 3D network of the pores, the kerogen/mineral phases, and crack networks and flow channels of oil shale samples were imaged before and after pyrolysis. At a voxel resolution of 60 nm (XNT), individual grains were identified. The image digitalization of the oil shale sample allows us to better define the porous network structures that evolve during pyrolysis. Based on the reconstructed multiscale X-ray CT data for the Mahogany oil shale drill core sample before pyrolysis, lamellar structures (kerogen-rich and silicates-rich) were observed and the distribution of the kerogen phase was identified. Crack networks, developed during the pyrolysis process, were evident and could be well defined. Two distinct regions with different size of cracks and voids were identified. Cracks and voids as small as 100 nm (from XNT images) were observed inside the silicate-rich lamellar structure while larger, anisotropic cracks and voids developed inside the kerogen-rich lamellar structure (from high resolution X-ray micro CT or HRXMT). These results validate results obtained from optical microscopy where different minerals are distributed in very thin and parallel laminae.

In addition, oil shale core samples after pyrolysis at three reaction temperatures (300^{o}C, 350^{o}C, and 400^{o}C) and heating rates of 1, 10 and 100 ^{o}C/min were imaged using HRXMT to establish the pore structure of the core after reaction (~5 micron voxel resolution). The porosity variation with drill core sample height as measured from the CT data clearly correlates with position of the kerogen layers. The mean porosity of the silicate-rich layers inside the reacted core is about 10% for the heating rates of 1 and 100^{o}C/min. However, for a heating rate of 10^{o}C/min, the mean porosity of the silicate-rich layers inside the reacted core is about 20%. The significant difference in the mean porosity may be attributed to a thermocouple drill hole for the sample with a heating rate of 10 ^{o}C/min. It should be noted that the reported porosity may be overestimated since residual kerogen and kerogen reaction products may be included.

Once the digital representation of the pore space was established, the Lattice Boltzmann Method (LBM) was used to calculate flow properties such as absolute and relative permeabilities of the pore network structure within +/- 10%. For example, the small cracks and voids inside the silicate-rich lamellar structure (seen in XNT images) were created due to thermal expansion of grain boundaries. Based on the LB simulation for saturated flow through the pore space inside the silicate lamellar structure after pyrolysis, the nature of the flow channels and the velocity scale were obtained. The estimated permeability from LB simulation of oil shale after pyrolysis was found to be about 0.00363 μm^2 or 0.363 millidarcy (mD). On the other hand, the absolute permeability was highly anisotropic inside the kerogen-rich lamellar structure. The estimated permeability was 3.87×10^{-8} cm^2 or 3.87 darcy, which is four orders of magnitude higher than that in the silicate-rich region. Anisotropic features of oil shale permeability are being quantified and may be the first 3D imaging of pyrolyzed oil shale by HRXMT and XNT.

TABLE OF CONTENTS

LIST OF FIGURES

LIST OF TABLES

1 Introduction

There is renewed interest in unconventional fuel resources as oil prices climb into hitherto unchartered territory. Unconventional oil resources are defined as extra heavy oils and bitumens associated with oil sand deposits and as kerogen associated with oil shale resources. Most of the world's known oil sand and oil shale deposits are in North America, and the combined potential from these resources far exceeds the world's known conventional oil reserves. The most significant oil shale deposits are in the Green River Formation of Colorado, Utah, and Wyoming, with an estimated resource size of 1.5-1.8 trillion barrels. These oil shale resources will be used primarily for producing transportation fuels. In a carbon-constrained world, transportation fuel production from these resources will require an understanding of processes that occur over a wide range of length and time scales from the structure of kerogen and how its binds to an inorganic matrix to the fluid flow resulting from in-situ processing of an oil shale interval that covers hundreds of acres. In this regard, parameters which are important for the analysis of the in-situ pyrolysis processing of oil shale include:

1. Kerogen conversion to oil, gas and coke
2. Nature of the pore space before and after pyrolysis
3. Porous media characteristics after pyrolysis
4. Permeabilities, and
5. Relative permeabilities.

In this report, we will describe approaches to address the very challenging characterization problems of items 2 to 5. To improve our understanding of transport phenomena of the in-situ pyrolysis processing of oil shale, the pore scale analysis of oil shale during pyrolysis at different temperatures is critical. In this work, the pore space of the oil shale samples before and after pyrolysis is characterized and digitized using multi-scale, non-invasive, non-destructive 3D imaging techniques of X-ray micro computed tomography (XMT) and X-ray nano computed tompgraphy (XNT). Once the digital representation of the pore space is established, the Lattice Boltzmann method (LBM) is used to calculate flow properties such as permeability of the pore network structure within (+/- 10%).

2 Experimental Methods

2.1 Sample preparation

Mahogany oil shale drill core samples (1.9 cm diameter) obtained from the Green River Formation in eastern Utah were used for this study. Selected oil shale core samples were pyrolyzed at different temperatures and heating rates. Multiscale 3D X-ray computed tomography (CT) imaging was used to characterize and to analyze the nature of the pore network structure before and after pyrolysis. In addition, thin-section samples were prepared for optical

microscopy and SEM analysis. Mineral compositions of the oil shale samples were determined using X-ray diffraction analysis.

2.2 Pyrolysis of oil shale core samples

Figure 1 shows the schematic of the pyrolysis experiment for cylindrical oil shale core samples (1.9 cm in diameter). A 15 cm long core was loaded in the pyrolysis reactor. The core was heated from the outside using a band heater. A prescribed heating rate was used to get to the reaction temperature, where the core was held for 24 hours. Nitrogen flowed at a steady rate of 55 ml/min during the experiment. The condensate was collected in a series of two condensers held at -6^{o}C. The core was cooled to ambient temperature, removed from the reactor and subjected to CT analysis as described.

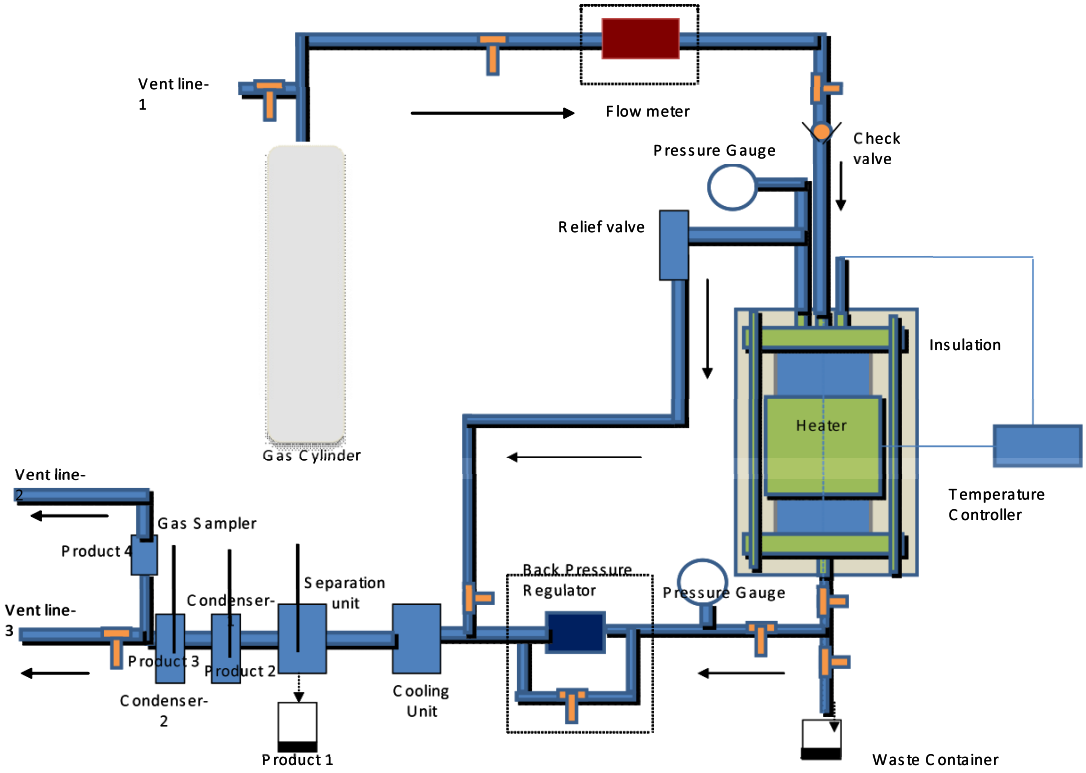

Figure 1. Schematic of the pyrolysis experiment for oil shale drill core samples.

2.3 Multiscale XMT/XNT

The pore structure and the connectivity of the pore space are important features which determine fluid flow in oil shale during pyrolysis. The XMT/XNT technique is the best non-invasive, non-destructive method available today to characterize complex pore structures. Cone beam XMT systems, introduced commercially a decade ago, are a valuable tool for 3D visualization,

characterization and analysis of multiphase systems at a voxel (volume element) resolution of 10 microns (μm), which corresponds to the ability to describe mineral structure and composition of multiphase particles having a size on the order of 100 μm (Miller and Lin, 2004). Most of the commercial XMT systems are based on the principle of point projection of an X-ray source through the sample onto a detector. In this design, the achievable resolution is a function both of the X-ray source size and of the detector resolution. The resolution is thought to be driven by the X-ray source spot size. The conclusion is that for conventional X-ray systems with large detector pixel sizes, a large geometric magnification combined with a small source spot size are required to achieve high resolution. The highest achievable resolution for these systems is limited by the spot size and the closest distance that can be allowed between the sample and the source. As a consequence, traditional XMT systems use transmission type sources to achieve a small source spot size combined with a minimal distance between sample and source.

The proximity of the sample to the source imposes a severe restriction on high-resolution tomography; for extended samples, the minimum distance between source and sample can be large, leading to a limited resolution. One possible solution for obtaining high resolution is to relax the restriction of the sample being close to the source by utilizing an X-ray detector with high resolution. With such a detector, an imaging resolution better than the X-ray source spot size can be realized for sources with spot sizes larger than the X-ray detector resolution. Such a system is the high-resolution X-ray micro CT (HRXMT) from Xradia (2010), which employs an X-ray detector with sub-micron resolution combined with a microfocus X-ray source that corresponds to a voxel resolution of 1 μm. This system has the ability to describe the structure and composition of multiphase particles having a size on the order of 10 μm. In this system, working distances between source, sample and detector are typically around 100 mm, so that full tomography even for larger samples can be achieved.

In addition to the XMT/HRXMT, further resolution is possible using the XNT scanner (Xradia, 2010), which provides two key improvements: (1) over one order of magnitude resolution gain to at least 60 nanometers (nm); and (2) a Zerneke phase-contrast imaging mode that dramatically enhances the contrast of low-density features.

In this study, 3D pore network structure for selected oil shale resources before and after pyrolysis have been characterized non-invasively at varying resolution from tens of microns down to 60 nm using XMT, HRXMT and XNT imaging techniques.

2.4 Lattice Boltzmann Method – pore scale modelling of single phase fluid flow

Unlike conventional computational fluid dynamics (CFD) methods, which involve a ‘top-down’ approach based on discretization of macroscopic continuum

equations, LBM (Qian et al., 1992 ; Chen, 1993; Shan and Chen, 1993; He and Luo, 1997; Stockman, 1999 ; Wolf-Gladrow, 2000; Succi, 2001; Sukop and Or, 2003) is based on a 'bottom-up' approach where constructed kinetic models incorporate microscopic model interactions and mesoscopic kinetic equations so that the macroscopic averaged properties of the flow obey the desired macroscopic equations. The resulting macroscopic, dynamic behavior is the result of the collective behavior of the microscopic particles in the system.

The LBM has received increasing attention in the area of fluid flow simulation in porous media (Martys and Chen, 1996; Lin and Miller, 2004) due to several attractive features, including its ability to incorporate molecular level interactions and a structure that facilitates code parallelization. In fact, over the last decade, the LBM has become an emergent mathematical technique able to handle the complex boundary conditions needed for flow in porous structures such as oil shale samples in a reasonable amount of time. It is also becoming popular for its capabilities to incorporate additional physical complexities such as multicomponent and multiphase flow (Chen & Doolen, 1998). Computer simulation can then be used to calculate macro variables, such as absolute and relative permeabilities, of the flow (Videla, Lin and Miller, 2008).

2.5 Forces considered for LBM of multiphase flow in porous media

The flow of two immiscible fluids simultaneously sharing the complex pore space in porous media is governed by the forces acting on the fluids, including pressure, viscous, gravitational, inertia and interfacial surface forces. The relative importance of each of these forces is usually characterized by the Reynolds (Re), Bond (Bo), and Capillary (Ca) numbers, as well as the viscosity ratio (M) as defined in equations 1 through 4, respectively.

$$\mathrm{Re} = \frac{u \cdot D}{\nu} \tag{1}$$

$$Bo = \frac{g\left(\rho_{nw} - \rho_{w}\right) \cdot R^2}{\gamma} \tag{2}$$

$$Ca = \frac{\nu_w \mu_w}{\gamma} \tag{3}$$

$$M = \frac{\mu_{nw}}{\mu_w} \tag{4}$$

Here, u is the velocity, D is the characteristic length, ν is the kinematic viscosity, R is characteristic length, g is gravitational acceleration, $\rho_{nw} - \rho_w$ is the density difference of non-wetting and wetting fluids, γ is the interfacial tensions between fluids, and μ is the viscosity.

In general, flow in porous media is dominated by the capillary forces, pressure and viscous forces are proportional to the rate of flow, and inertia forces are negligible. Because the pressure and viscous forces depend on the flow rate, the capillary and gravitational forces become more important when the rate of flow is slower.

2.5.1 Capillary Pressure

When two immiscible fluids are in contact in the porous medium, a discontinuity in pressure exists across the interface. This difference in pressure is called the capillary pressure, defined as the difference between the pressures of the non-wetting fluid p_{nw} and the wetting fluid p_w as shown in equation 5.

$$p_c = p_{nw} - p_w \tag{5}$$

Figure 2 shows a curved interface between two immiscible fluids under static equilibrium. From the figure it is observed that capillary pressure depends on the curvature of the interface. In soil science, the negative of the capillary pressure is known as tension or suction head.

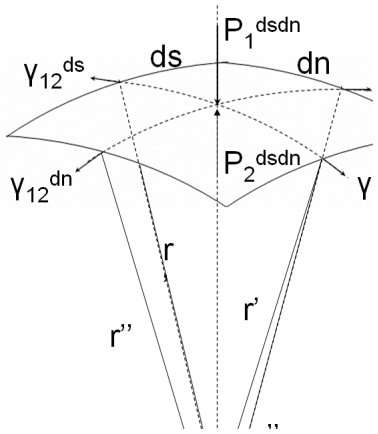

Figure 2. Forces acting on the elementary surface around a point of a curved interface between two immiscible fluids at static equilibrium.

Interfacial shapes in static and quasi-static situations are governed by the Laplace equation. By applying the condition of mechanical equilibrium for the forces acting on the interface, Laplace showed that the capillary pressure is proportional to the interfacial tension and inversely proportional to the curvature of the meniscus. Laplace's law is presented in equation 6 for a 3D pore structure and is dependent on the interfacial tension γ_{12} and the radii of curvature, r^*.

$$p_2 - p_1 = p_c = 2\frac{\gamma_{12}}{r^*} \text{ , with } \frac{1}{r^*} = \frac{1}{2}\left(\frac{1}{r'} + \frac{1}{r''}\right) \quad (6)$$

2.5.2 Interfacial Tension and Contact Angle

Porous structures involve the presence of a solid phase which, in a capillary system, interacts with at least two fluid phases. As a result, there are at least three surfaces subjected to surface tension as shown in Figure 3. The static equilibrium between the three interfacial tensions leads to the well known Young's equation shown in equation 7.

$$\gamma_{\mathrm{lg}} \cos\theta = \gamma_{sg} - \gamma_{sl} \quad (7)$$

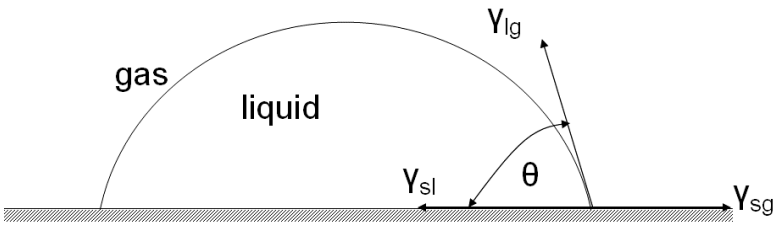

Figure 3. Static equilibrium between the three interfacial tensions at the solid surface.

The contact angle is normally used to describe the preferential characteristics of the solid surface to be wet. In some cases, no equilibrium is possible $\left(\gamma_{\mathrm{lg}} > \gamma_{sg} - \gamma_{sl}\right)$ and the liquid covers the whole surface completely. In such cases, the liquid is said to wet the solid perfectly.

2.5.3 Capillary Pressure versus Saturation Curves

The capillary pressure depends on the saturation, interfacial tension, wetting angle, viscosity ratio and Bond number (Marle, 1981). Because the capillary pressure depends on the contact angle, one may expect a hysteresis effect, meaning that different capillary pressure–saturation curves are obtained depending on the history of the fluid motion. For example, the capillary pressure–saturation curve may depend on whether a sample was initially saturated with the wetting or non-wetting fluid component. If the sample is initially saturated with the wetting fluid, an increment of the capillary pressure produces the displacement of the wetting fluid by the non-wetting fluid in a process known as drainage. If the

sample is initially saturated with the non-wetting fluid, a decrease in the capillary pressure produces imbibition, the displacement of one fluid by another immiscible fluid. Figure 4 shows a typical curve which reveals the relation of capillary pressure to saturation. The entry point P* shows that if a sample is initially saturated by a wetting fluid, a certain pressure, the so called threshold pressure or non-wetting entry value, must be built up before the non-wetting fluid begins to penetrate the sample. The figure also shows that at high capillary pressure the wetting saturation reaches a minimum limit, the so-called irreducible saturation of the wetting fluid S_{w0}. The imbibition curve shows that a maximum limiting saturation value is reached at zero capillary pressure. This point corresponds to the residual saturation S_{nw0} of non-wetting fluids that stay entrapped in the porous solid. It is well known that pressure–saturation curves are subject to hysteresis phenomena. Therefore, the capillary pressure is a function of the direction of displacement and the history of the two-phase flow in the porous sample.

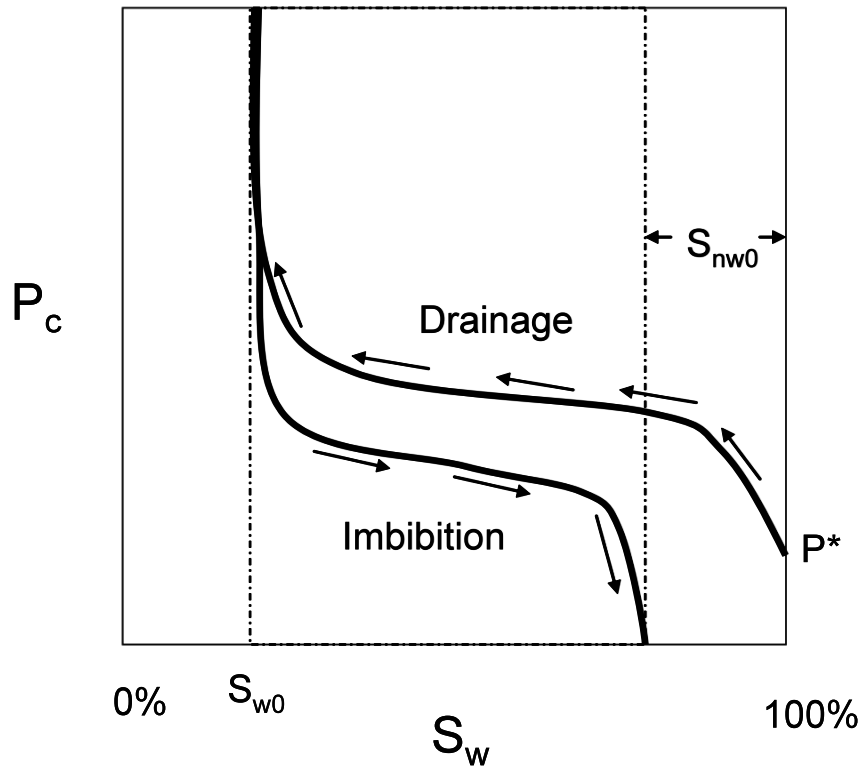

Figure 4. Typical capillary pressure curve.

3 Results and Discussion

The oil shale drill core samples are very hard and fine grained, showing a laminated structure composed mainly of dolomite, calcite and quartz with some clay minerals (illite and kaolinite) in different percentages. These clay minerals exhibit good crystallinity as indicated from X-ray diffraction analysis. Also, the SEM analysis indicates the presence of gypsum and pyrite minerals.

The optical microscopy analysis of the thin sections of oil shale samples, as shown in Figure 5, confirm the lamellar structure in which different minerals are distributed in very thin and parallel laminae. These laminae include alternating layers of clay minerals and carbonate minerals. The iron oxides and organic matter give color to the banding structure. Both iron oxide and organic matter are mostly associated with the clay mineral layers. Occasionally, they are associated with the carbonate layers. The carbonate minerals are microcrystalline. The clay mineral layers range in thickness from 20 to 30 μm, while the carbonate mineral layers range in thickness from 10 to 20 μm. The quartz mineral is of silt size and found as elongated particles parallel to the banding structure of the oil shale.

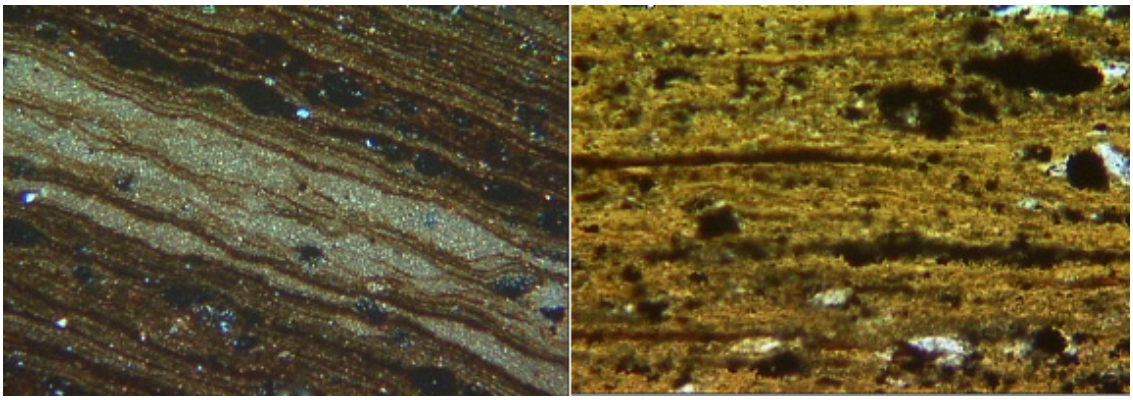

Figure 5. Micrograph of the Mahogany oil shale drill core sample. Left: alternating carbonate layers and clay layers with kerogen distribution especially in the clay layers (crossed polarized light). Right: organic matter is mostly associated with the clay layers (plane polarized light).

3.1 Multiscale XMT/XNT – before pyrolysis

Using a combination of XMT/XNT and specialized software, the 3D network of the pores, kerogen/mineral phases, crack network and flow channels of oil shale samples can be imaged before and after pyrolysis. The image digitalization of the oil shale samples allows us to obtain the porous network structure that evolves during pyrolysis. Figure 6 shows the 3D volume rendered images from the reconstructed multiscale X-ray CT data for the Mahogany oil

shale drill core sample before pyrolysis. The sample was imaged first with XMT at 39 μm voxel resolution, followed by HRXMT at 1 μm voxel resolution, and finally by XNT at 60 nm voxel resolution. Gray scale level indicates variations in the X-ray attenuation coefficients that depend on the density and atomic number of material within each voxel. Lamellar structures (kerogen-rich and silicate-rich layers) are observed. The kerogen–rich layers are the dark colored region while the mineral-rich (silicate in the form of dolomite) layers are the light colored regions. The middle column shows the distribution of the kerogen phase. These results further validate results obtained from optical microscopy, which showed different minerals distributed in very thin and parallel laminae (see Figure 5). At a voxel resolution of 60 nm (XNT), individual grains can be identified easily.

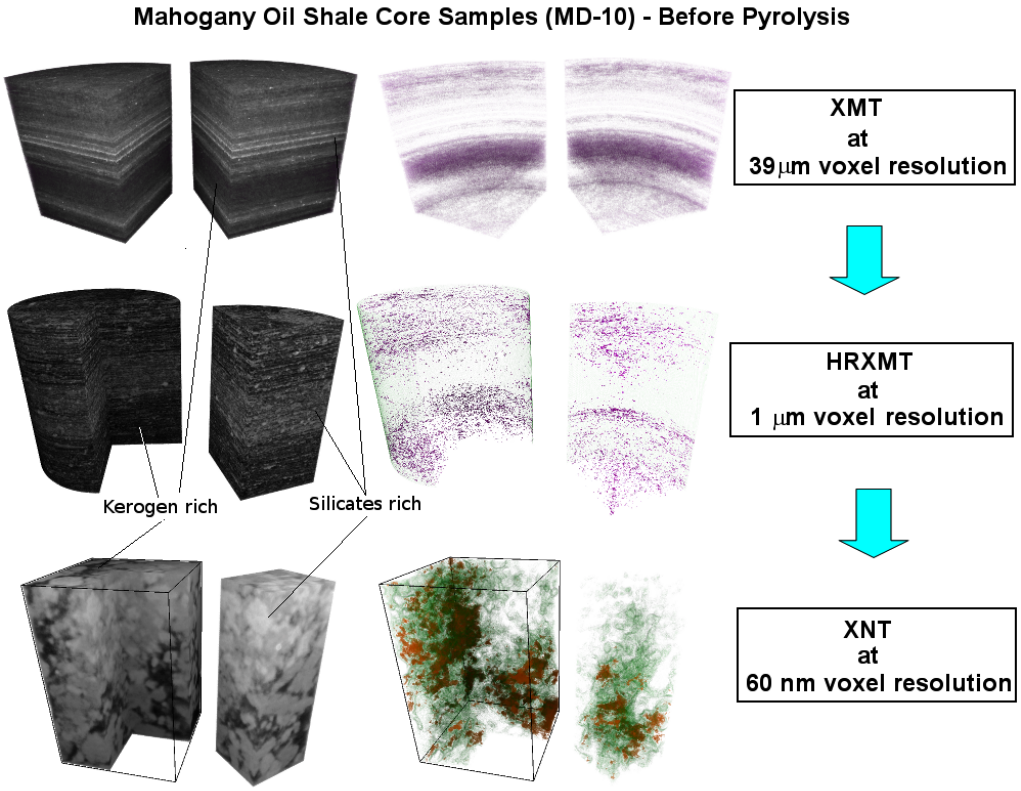

Figure 6. Volume rendered images of Mahogany oil shale drill core sample MD-10 from reconstructions of multiscale X-ray CT data including XMT at 39 μm voxel resolution, HRXMT at 1 μm voxel resolution and XNT at 60 nm voxel resolution. The middle column shows the distribution of the kerogen phase (in purple, purple and brown colors for XMT, HRXMT and XNT, respectively).

3.2 Multiscale XMT/XNT – after pyrolysis

Image digitalization of the oil shale samples allows us to obtain the porous network structure that evolves during pyrolysis. Figure 7 shows the 3D volume rendered images from the reconstructed multiscale X-ray CT data for a Mahogany oil shale drill core sample after pyrolysis (400°C, N_2 flow). Crack networks, developed during the pyrolysis process, are evident and can be well defined. Two distinct regions with different size of cracks and voids are identified. Cracks and voids as small as 100 nm (from XNT images) are observed inside region A (silicate-rich lamellar structure), However, larger, anisotropic cracks and voids are developed inside region B (kerogen-rich lamellar structure from HRXMT images) as seen in Figure 7. Figure 8 shows the tri-planar and volume rendered images of region A of the residual product after pyrolysis.

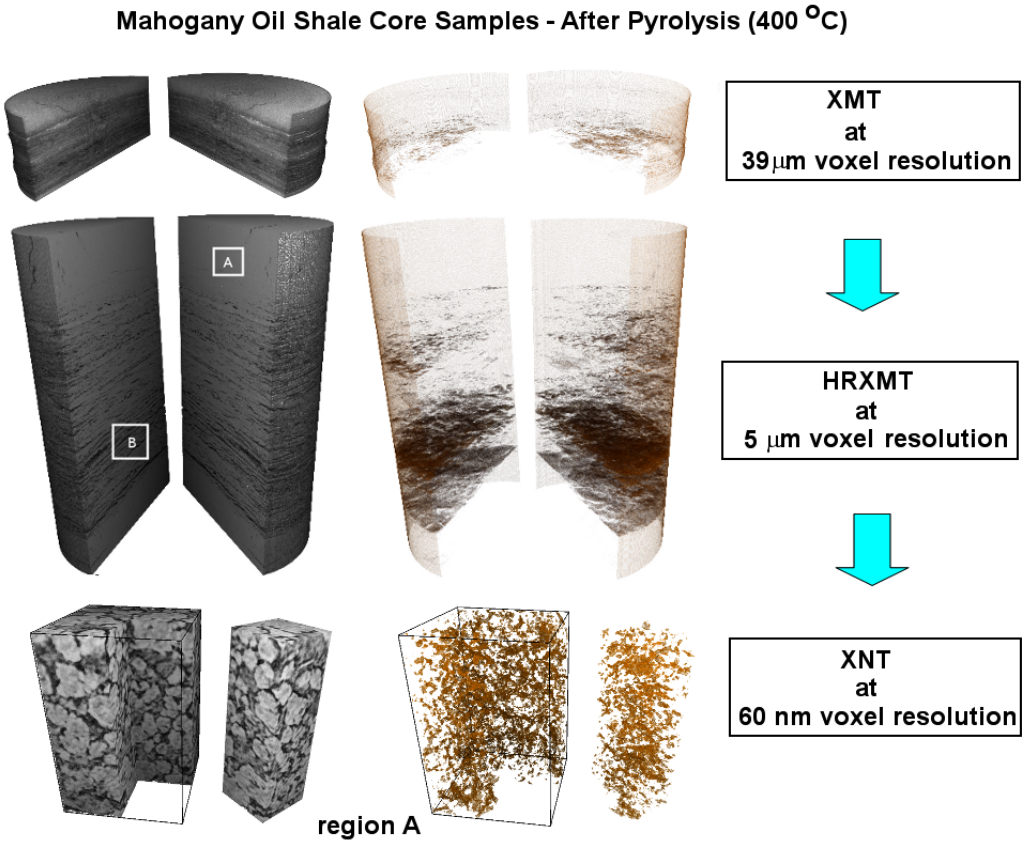

Figure 7. Volume rendered images of Mahogany oil shale drill core sample after pyrolysis (400°C, N_2 flow) from the reconstructions of multiscale x-ray CT data including, XMT at 39 μm voxel resolution, HRXMT at 5 μm voxel resolution and XNT at 60 nm voxel resolution.

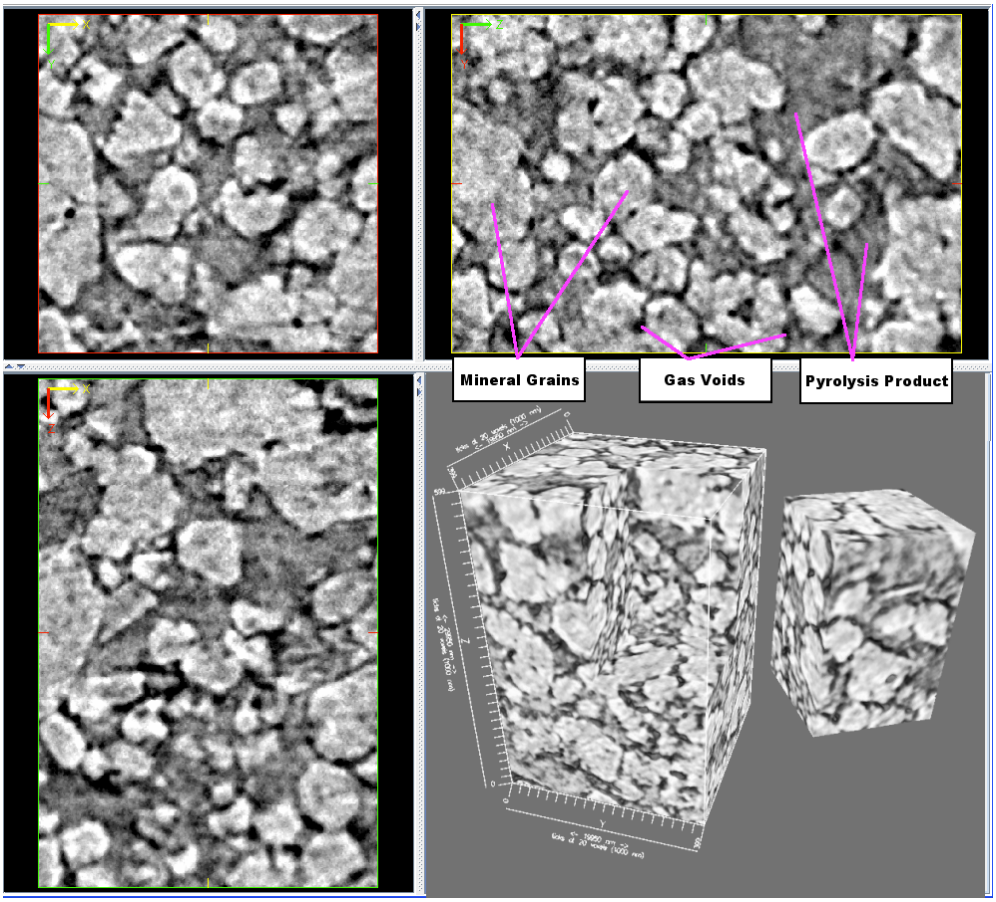

Figure 8. Triplanar and volume rendered images of region A of Mahogany oil shale drill core sample (sample volume = 20x20x30 μm) after pyrolysis at 400°C.

3.3 Geometric analysis of pore network structure after pyrolysis at different heating rates

A 15 cm long core of indicated diameter (see Table 1) was loaded in the pyrolysis reactor. The core was heated from the outside using a band heater. A prescribed heating rate was used to get to the desired reaction temperature, where the core was held for 24 hours. Nitrogen flowed at a steady rate of 55 ml/min during the experiment. The condensate was collected in a series of two condensers held at -6°C. The core was cooled to ambient temperature, removed

from the reactor and subjected to HRXMT analysis as described. To investigate the effect of reaction temperature, drill core of oil shale samples were pyrolyzed at different temperatures and the conditions are summarized in Table 1.

Table 1. Pyrolyzed oil shale samples examined at three different reaction temperatures and different heating rates.

Sample No.	Type	Heating Rate(^{o}C/min)	Misc
MD-3	¾" drill core	100	N_2 flow, 300^{o}C
MD-4	¾" drill core	100	N_2 flow, 350^{o}C
MD-5	¾" drill core	100	N_2 flow, 400^{o}C
MD-11	1" drill core	1	
MD-12	1" drill core	10	Drill hole at center of core for thermocouple wire

The image digitalization of the oil shale samples allows us to obtain the pore network structure that evolved during pyrolysis at different heating rates. Figure 9 shows photos of the reaction cores subjected to various heating rates that were used for the HRXMT analysis. The FOV (field of view) regions are about 5 mm^3 inside the center of the reaction core with the exception of the core sample at the 10^{o}C/min heating rate. There, FOV focused on the wall region between the central drill hole and edge of the core.

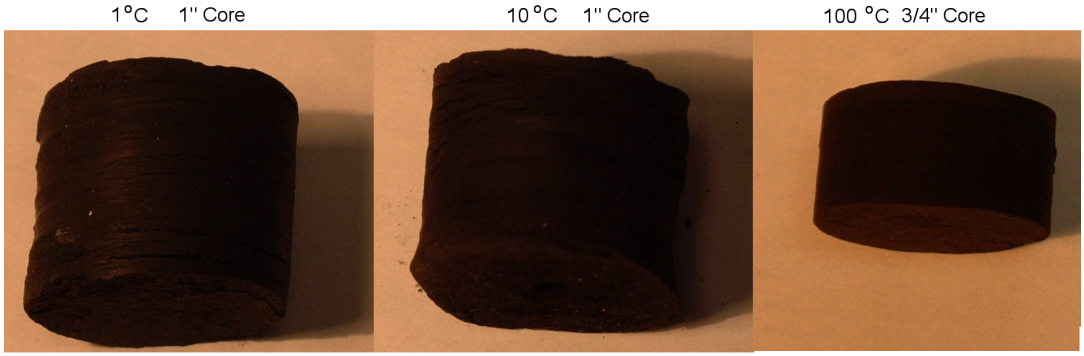

Figure 9. Reaction cores subjected to different heating rates (1, 10 and 100^{o}C/min) prior to HRXMT analysis. The center reaction core has a drill hole at the central region of the core for insertion of the thermocouple wire.

The 3D volume rendered images from the reconstructed X-ray CT data (~5 micron voxel resolution) for the Mahogany oil shale drill core samples after pyrolysis at different heating rates are shown in Figure 10. Crack networks, developed during the pyrolysis process, are evident. Two distinct regions with

different sizes of cracks and voids are identified. The dark region shows the void space (cracks and pores) and the residual kerogen. The light region shows the layers of mineral matter (clay and carbonates).

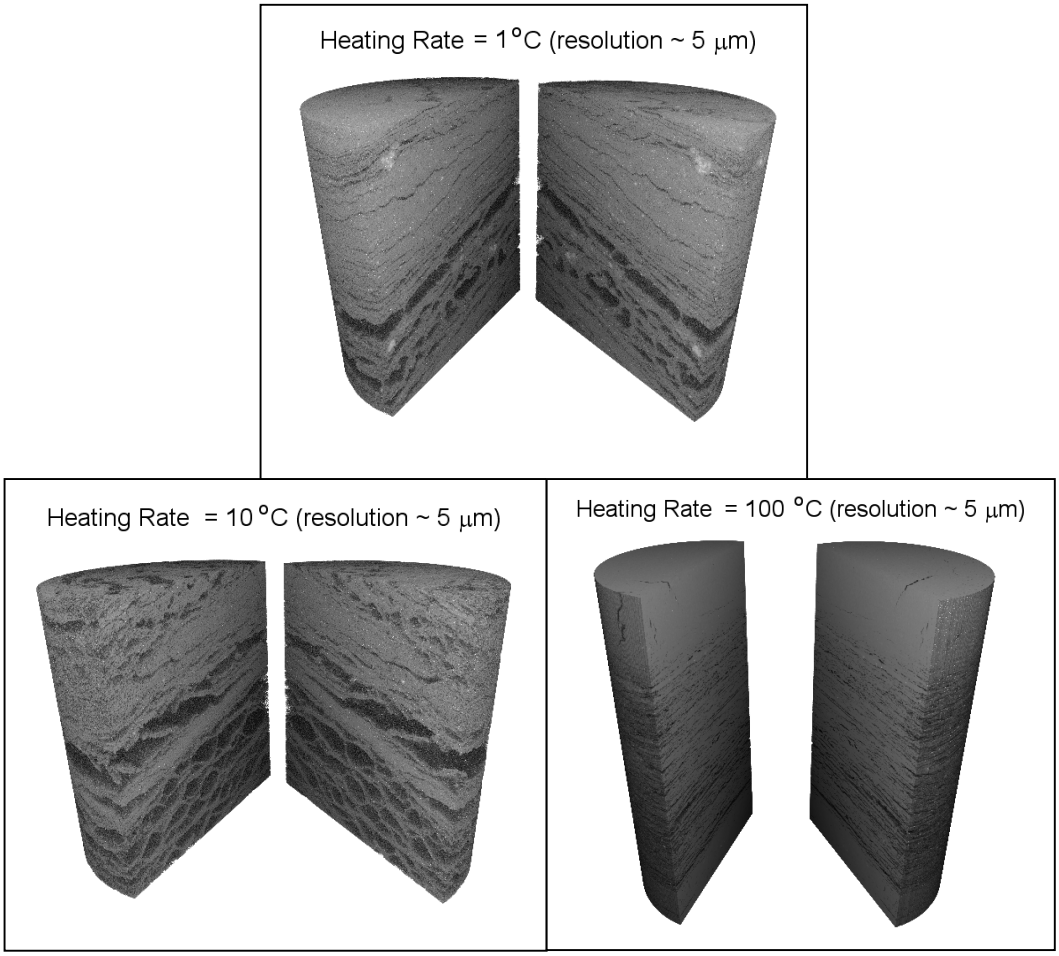

Figure 10. Volume rendered images of Mahogany oil shale drill core samples after pyrolysis at different heating rates (1, 10 and 100°C/min). Images are from the reconstructions of HRXMT data at ~5 μm voxel resolution. Gray scale level indicates variations in the X-ray attenuation coefficients which depend on the density and atomic number of material within each voxel. Cracks and voids are observed in the kerogen-rich lamella layers/dark regions. The light regions are the silicate-rich lamella layers.

Porosity, the simplest property of such porous structures, is defined as the volume fraction of pores. Porosity can be used to predict the permeability defined by Darcy's law. The porosity of oil shale after pyrolysis can be used to predict the permeability for pore-scale network modeling or from Lattice-Boltzman simulations as reported previously. In addition, information such as porosity

change after pyrolysis at different reaction temperatures/heating rates can be used as inputs to models of in-situ thermal treatment of oil shale and oil sands.

Quantitative information on porosity changes of oil shale samples after pyrolysis can be determined from the CT data. To facilitate the pore geometry analysis, the bottom portions of the original gray scale CT image data (512x512x512 voxel) were treated to extract the pore features from the images shown in the left-hand side of Figures 11, 12 and 13 for samples MD-3, MD-4 and MD-5, respectively. In this manner, the porosity was measured as the pore voxel volume divided by the total voxel volume of the 3D data set. Note that the porosity includes unreacted kerogen. The spatial separation of the residual kerogen from the actual pore is to be accomplished in future analysis.

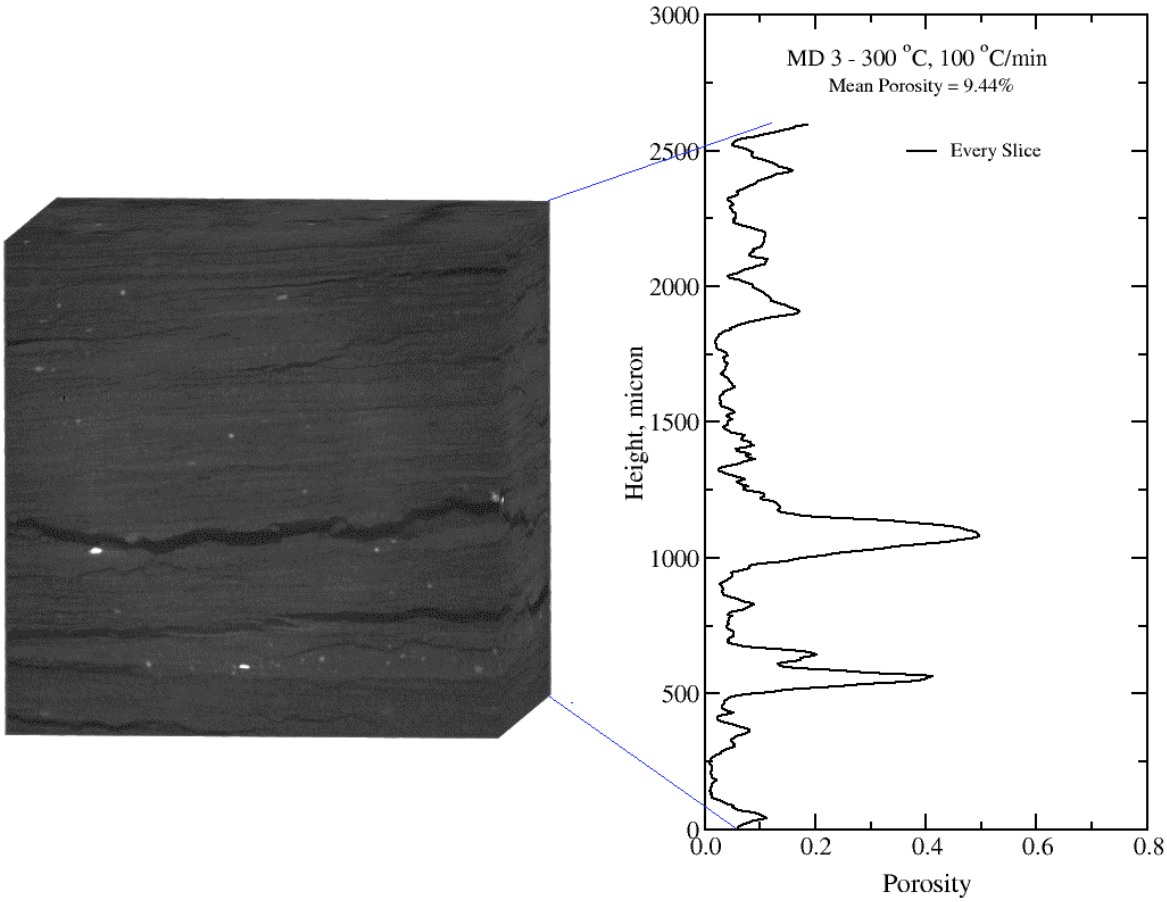

Figure 11. Overall view of the Mahogany oil shale drill core sample MD-3 after pyrolysis at a reaction temperature of 300°C and a heating rate of 100°C/min. Cracks and residual kerogen are identified by the black regions in the sample image on the left. The porosity variation with drill core sample height as measured from the CT data is shown on the right.

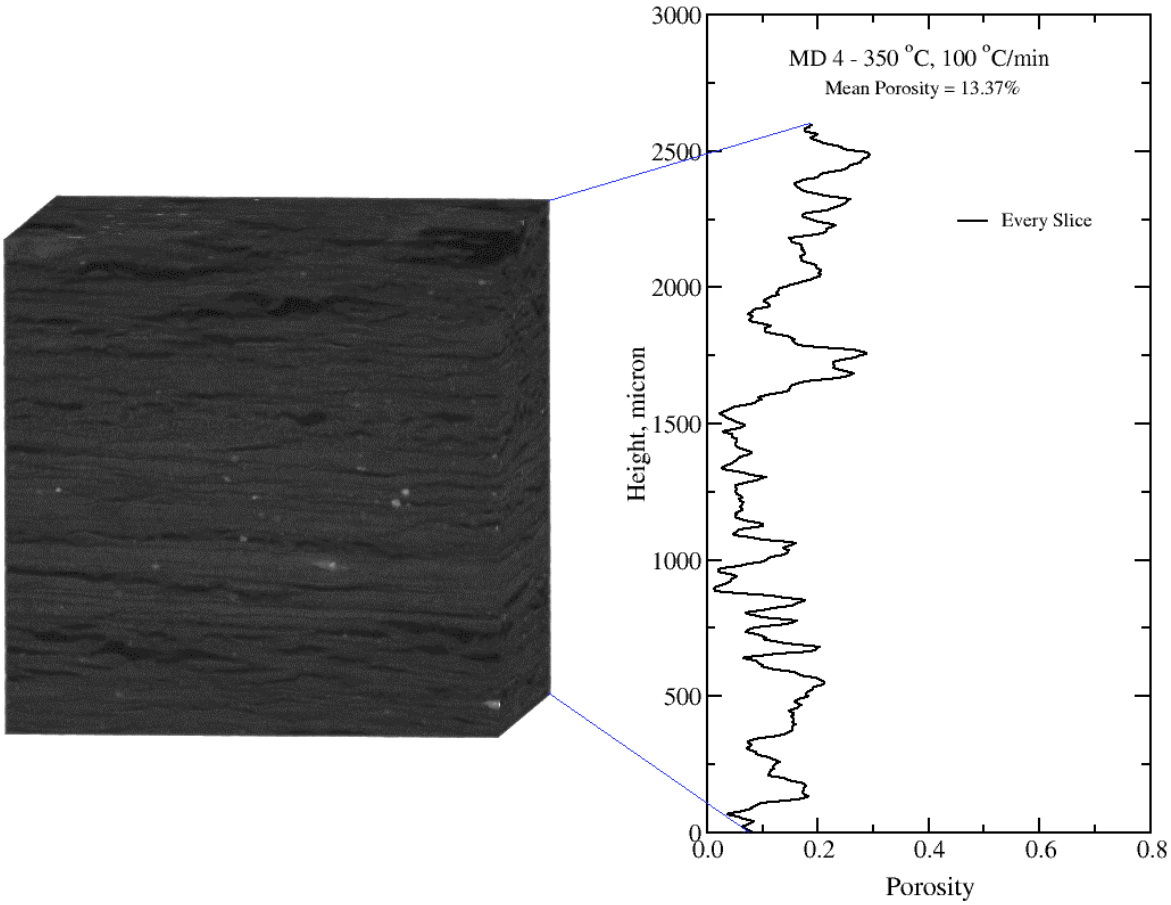

Figure 12. Overall view of the Mahogany oil shale drill core sample MD-4 after pyrolysis at a reaction temperature of 350°C and a heating rate of 100°C/min. Cracks and residual kerogen are identified by the black regions in the sample image on the left. The porosity variation with drill core sample height as measured from the CT data is shown on the right.

Figures 11, 12, and 13 provide the overall views of the oil shale drill core samples after pyrolysis at reaction temperatures of 300°C (MD-3), 350°C (MD-4), and 400°C (MD-5) and a heating rate of 100°C/min. In addition, the porosity profiles measured from the CT data along the height of the drill core sample are plotted on the right-hand side of the figures. The porosity is defined as the ratio between the void area and the total area of each cross section. As expected, higher-porosities are obtained from the kerogen-rich layer of the pyrolyzed oil shale drill core samples. Table 2 summarizes the mean porosity change after pyrolysis at a heating rate of 100 °C/min.

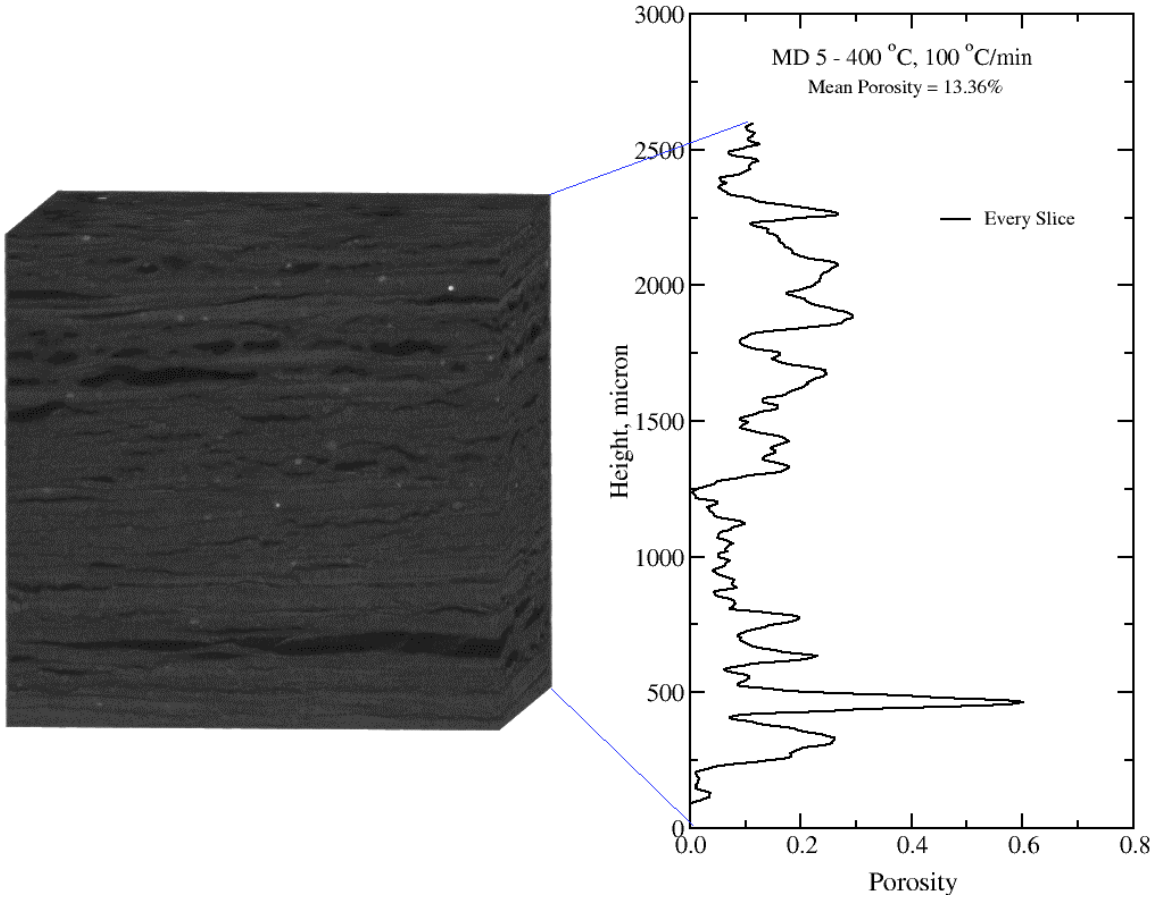

Figure 13. Overall view of the Mahogany oil shale drill core sample MD-5 after pyrolysis at a reaction temperature of 400°C and a heating rate of 100°C/min. Cracks and residual kerogen are identified by the black regions in the sample image on the left. The porosity variation with drill core sample height as measured from the CT data is shown on the right.

Table 2. Mean porosity for the pyrolyzed oil shale cores at different reaction temperatures.

Sample No.	Temperature (°C)	Heat Rate (°C/min)	Mode	Mean Porosity (%)
MD-3	300	100	N_2 flow	9.44
MD-4	350	100	N_2 flow	13.37
MD-5	400	100	N_2 flow	13.36

Figures 14 and 15 illustrate the overall views of the 1” oil shale drill core samples and the corresponding porosity profiles measured from the CT data along the height after pyrolysis at heating rates of 1 and 10°C/min, respectively. The porosity is defined as the ratio between void area and the total area of each cross section. As expected, higher porosities are obtained for the kerogen-rich layer of the pyrolyzed oil shale drill core samples. The mean porosity change of the silicate-rich layers inside the reacted core is about 10% for both 1 and 100 °C/min heating rates. However, results from a heating rate of 10°C/min indicate higher mean porosity for the silicate-rich layers. It seems that the drill hole at the center of the core influenced the crack formation for the silicate-rich layers, increasing the mean porosity to 20%.

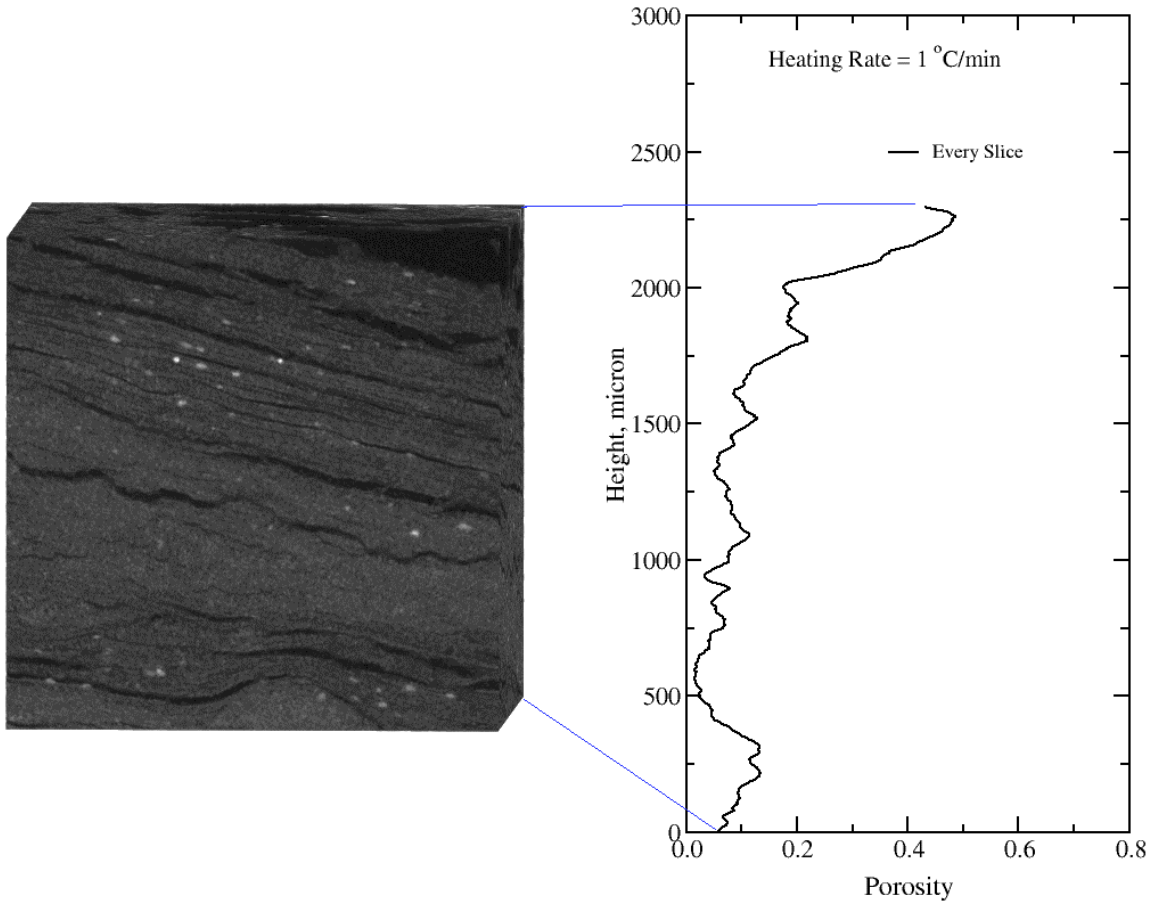

Figure 14. Overall view of the Mahogany oil shale drill core sample MD-11 after pyrolysis at a heating rate of 1°C/min. Cracks are identified by the black regions in the sample image on the left. The porosity variation with drill core sample height as measured from the CT data is shown on the right.

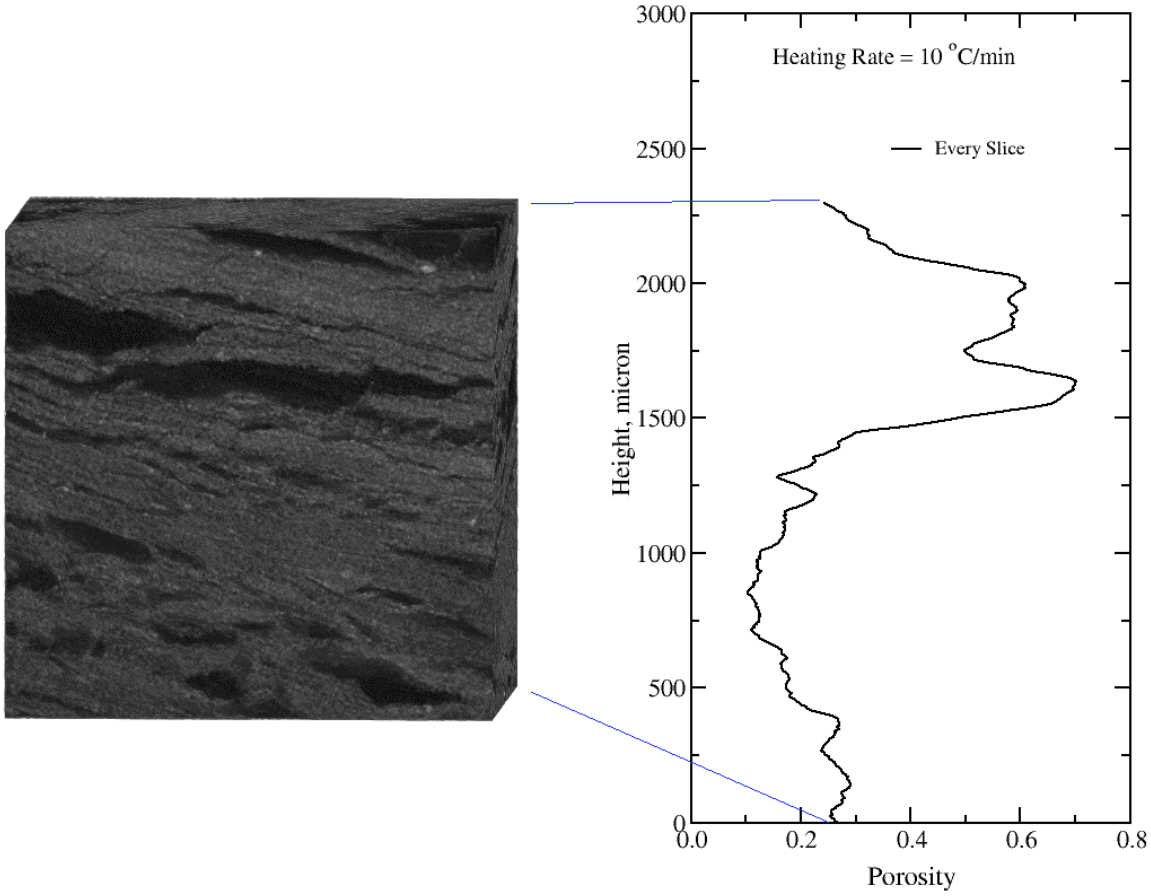

Figure 15. Overall view of the Mahogany oil shale drill core sample MD-12 after pyrolysis at a heating rate 10°C/min. Cracks are identified by the black regions in the sample image on the left. The porosity variation with drill core sample height as measured from the CT data is shown on the right.

3.4 LBM – pore scale modelling of single phase fluid flow

As indicated previously, the cracks and voids inside region A (silicate lamellar structure) of the oil shale pyrolysis product sample are small and are created due to thermal expansion of grain boundaries. Figure 16 illustrates the 3D view of the LB simulation for saturated flow through the pore space of Region A in sample MD-5 after pyrolysis. The right-hand side of Figure 16 shows the nature of the flow channels after the solid phase (white) is removed. The velocity scale is color-coded as shown by the color bar in Figure 16. Velocities range from black for no flow, through blue, green, yellow and finally red for the highest flow rate. The estimated permeability from LB simulation of oil shale after

pyrolysis is approximately 0.00363 mm^2 or 0.363 mD (millidarcy). On the other hand, it is noted that the absolute permeability is highly anisotropic, Figure 17 shows the 3D views of LB simulated flow along the x-axis through the reconstructed HRXMT image of Region B of MD-5 after pyrolysis. The estimated permeability is 3.87×10^{-8} cm^2 or 3.87 darcy, which is four orders of magnitude higher than that in region A.

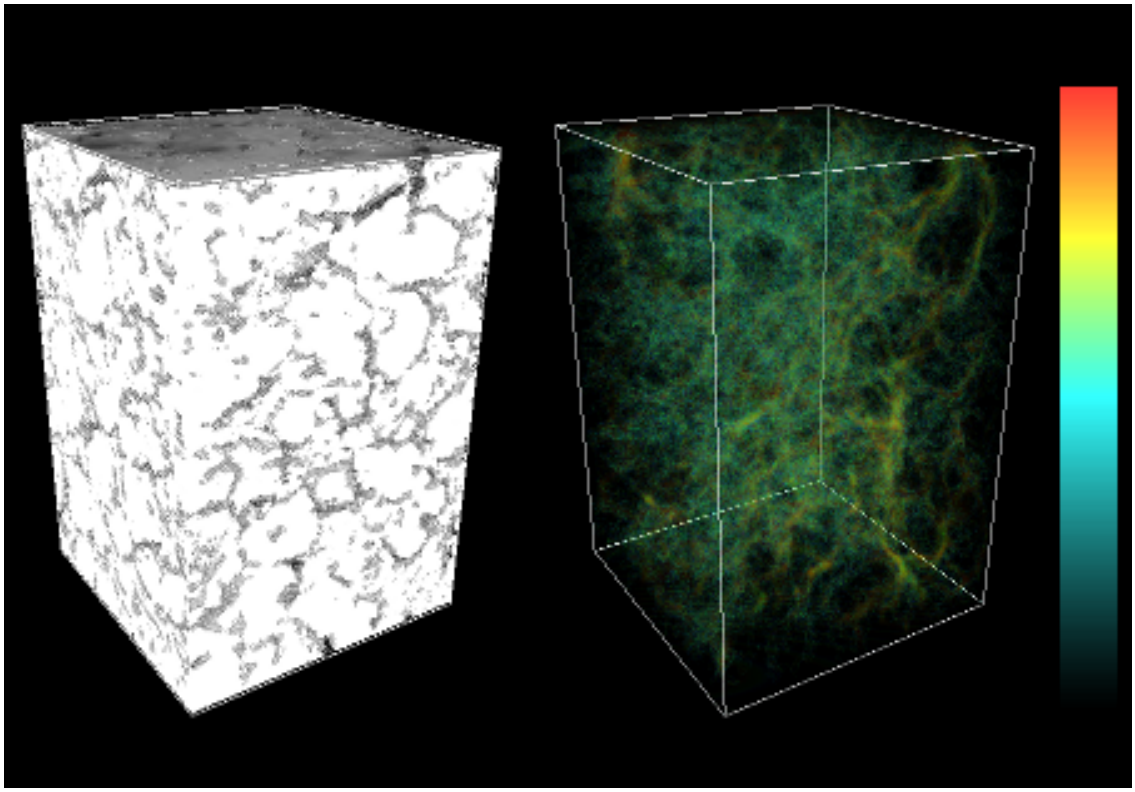

Figure 16. 3D views of LB simulated flow through the reconstructed XNT image of region A of the oil shale pyrolysis product prepared at 400°C. Left: solid phase as white. Right: transparent solid phase to reveal flow channels. The estimated permeability is 0.000363 μm^2 or 0.363 mD.

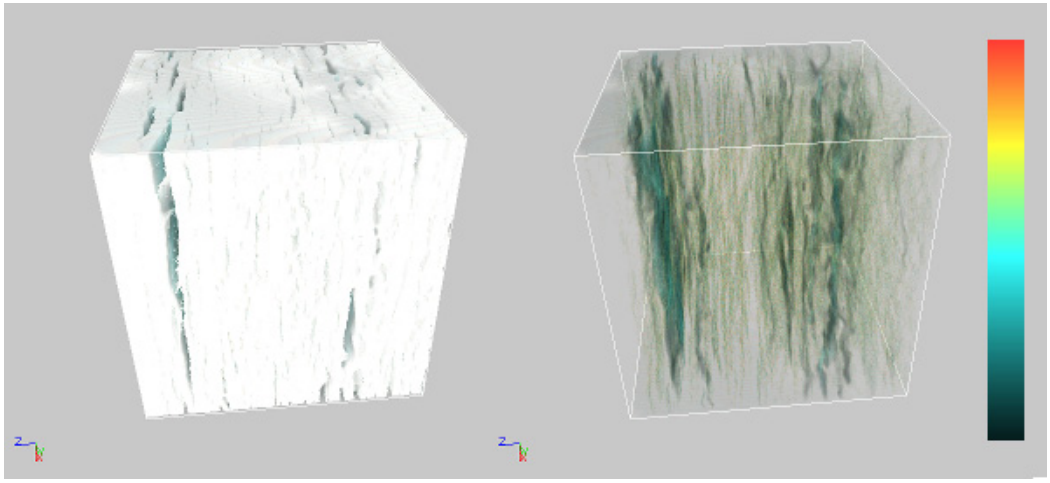

Figure 17. 3D views of LB simulated flow along x-axis through the reconstructed HRXMT image of region B of the oil shale pyrolysis product sample. Left: solid phase as white. Right: transparent solid phase to reveal flow channels (pore network structure after pyrolysis). The estimated permeability is 3.87×10^{-8} cm^2 or 3.87 darcy.

3.5 LBM – pore scale modeling of multiphase fluid flow

In the previous section, a single phase LBM model was used to estimate permeabilities in various regions of a pyrolyzed oil shale sample. While oil shale is layered and anisotropic, oil sands are not layered and isotropic. In this section, a multiphase LBM model is used to compute flow through two different oil sand samples.

3.5.1 The single component multiphase He-Chen-Zhang Model

In order to investigate the flow through the porous media, a multiphase LB fluid flow model is required. Several LB multiphase fluid flow models have been introduced in the past years for applications in areas of fluid dynamics such as phase separation (Rothman and Zaleski, 1991) and fingering phenomena in a channel (Kang et al, 2004). The major advantage claimed for pursuing the use of LBM instead of standard CFD methods resides in its ability to model complex solid boundaries in any arbitrary geometry, its suitability for code parallelization and its ability to incorporate microscopic force interactions that control the interface dynamics.

In general, the LBMs for multiphase flow can be described as single component or multicomponent models. Single component models describe phase separation by an equation of state that, below the critical temperature, automatically segregates phases into two stable densities: vapor (light density)

and liquid (heavy density). In this category, we found the single component Shan and Chen model (1993), the single component free-energy model (Swift et al., 1995,1996), and the He-Shan-Doolen model (He, Shan, Doolen, 1998) to be of interest. On the other hand, multicomponent models use one particle distribution function (PDF) and one evolution equation to represent each fluid component in the system and segregation is simulated by interaction between the two independent fluids. For further discussion and comparison of these methods the reader is referred to the work done by Chen and Doolen (1998) and He and Doolen (2002).

We start with a description of the single-component multiphase flow model developed by He, Chen and Zhang (1999). In their seminal work, they present a new multiphase model derived directly from discretizing the continuous kinetic equation for non-ideal fluids modified for incompressible flow. The He-Chen-Zhang model (1999), an extension of the He-Shan-Doolen model (1998), has not been used extensively and is not as popular as the Shan and Chen model. Videla (2009) has applied the model to 2D and 3D Rayleigh-Taylor instability simulations (He et al, 1999; Zhang et al, 2000) and has compared the data with theoretical values and results from a CFD simulation. The results show good qualitative and quantitative agreement.

Unlike traditional CFD methods that resolve the macroscopic governing equations using a free boundary surface approximation, the He-Chen-Zhang model simulates the interfacial dynamics such as phase segregation and surface tension from mesoscopic kinetic equations. In this model, the interfacial dynamics are the result of molecular interactions where two distribution functions are used, one for tracking the pressure and velocity, the other for tracking only the density. When the molecular attraction is strong enough, the fluid automatically segregates into two different phases. One of this model's major advantages is that, unlike the Shan and Chen model, the surface tension can be adjusted beforehand as a free parameter due to its thermodynamic consistency.

Theoretically speaking, the use of these equations of state should allow consideration of high density ratios for the single component multiphase system. However, as density ratios increase, the spurious velocity magnitudes also increase, making simulations numerically unstable. We have been able to run simulations with density ratios up to 30. Numerical instability is an area that requires more research in the whole area of LBM.

3.5.2 Simulation of fluid penetration and capillary phenomena in porous media

The solid-fluid interaction explained before can be extended to the analysis and simulation of two-phase flow in complex porous structures. First, the behavior of the LB model in simple capillary tubes is illustrated, then the model is

expanded for the simulation of fluid penetration in an actual 3D image of oil sand as obtained from XMT analysis.

In a capillary tube, there is fluid displacement when the flow is driven by a difference in pressure strong enough to overcome the capillary pressure. Figure 18 shows LB simulated results at the same final iteration step for capillary tubes where the non-wetting fluid displaces the wetting fluid (drainage process from left to right) for several driving pressure differences. From these images, it is possible to observe that the wettability of the wall, as defined by the wetting film parameter D_ρ, creates a wetting film at the surface which remains attached to the wall while the non-wetting fluid front advances. The width of this wetting film depends of the strength of the attraction and herein the result is about three lattice units.

Figure 18. Simulations of fluid displacement for increasing difference in pressure controlled by the density at the outlet. Values from top to bottom are: 0.2508, 0.2498, 0.2482 and 0.2466. D2Q9 lattice of size 35x130 lu^2. Parameters for simulations are $\bar{k}$=0.1, D_ρ=0.99 and $\rho_l/\rho_g = 10$ ($\bar{k}$ defines surface tension).

In LBM simulations, the difference in pressure between the inlet and outlet can be set by fixing the density of the fluids. These densities are related to the pressure by the equation of state. The entry pressure for displacement of one fluid by another in a porous capillary is a function of the radius (R) of the pore, the surface tension (γ) of the fluids, and the contact angle (θ). The entry pressure is given by equation 8.

$$P_{entry} = \frac{2\gamma \cos\theta}{R} \tag{8}$$

The capillary phenomenon of interest, similar to the network microstructure of the oil sands/oil shale, is the behavior of the system when two or more capillary tubes (throats) are present. We have taken the simplest case of two-phase flow of two porous channels of different diameters under the same pressure difference. As Figure 19 shows, one of the throats is six times smaller than the other and therefore has an entry pressure that is six times higher. The pressure across the phases has been set to be higher than the entry pressure for the bigger diameter throat but smaller than the entry pressure for the smaller diameter throat. In the sequence of images in Figure 19 (left to right and top to bottom), it is possible to observe the preferential flow that is developed by the meniscus, which invades the channel with the higher throat radius and smaller flow resistance.

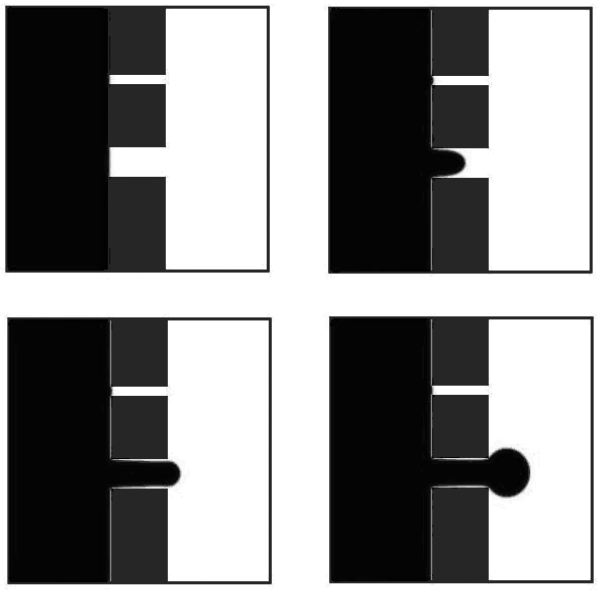

Figure 19. Simulations of fluid displacement in a capillary tube with two throats of different radii. Images from left to right and top to bottom show flow after: 1000, 10000, 20000 and 30000 iterations. D2Q9 lattice of size 35x130 lu^2. Parameters for simulations are $\bar{k}$=0.1, D=0.99 and $\rho_l / \rho_g = 10$ ($\bar{k}$ defines surface tension).

From these results, it is evident that this modified He-Chen-Zhang model has good qualitative agreement with theory for two-phase flow in porous media. In the following discussion, we proceed with application to actual porous network structures such as would be found in the pyrolysis of oil sand/oil shale.

Lenormand et al (1988) ran numerous network simulations and experiments performed in transparent etched networks to identify patterns and to describe percolation of a non-wetting fluid when injected into a medium saturated

with a wetting fluid. As an outcome of his research, Lenormand proposed a phase diagram for immiscible displacement characterized by the capillary number (eq. 3) and the viscosity ratio (eq. 4) as shown in Figure 20. Parameters γ , ν_w , μ_w and μ_{nw} are defined as interfacial tension, kinematic viscosity of the wetting fluid and the viscosities of the wetting and non-wetting fluids, respectively.

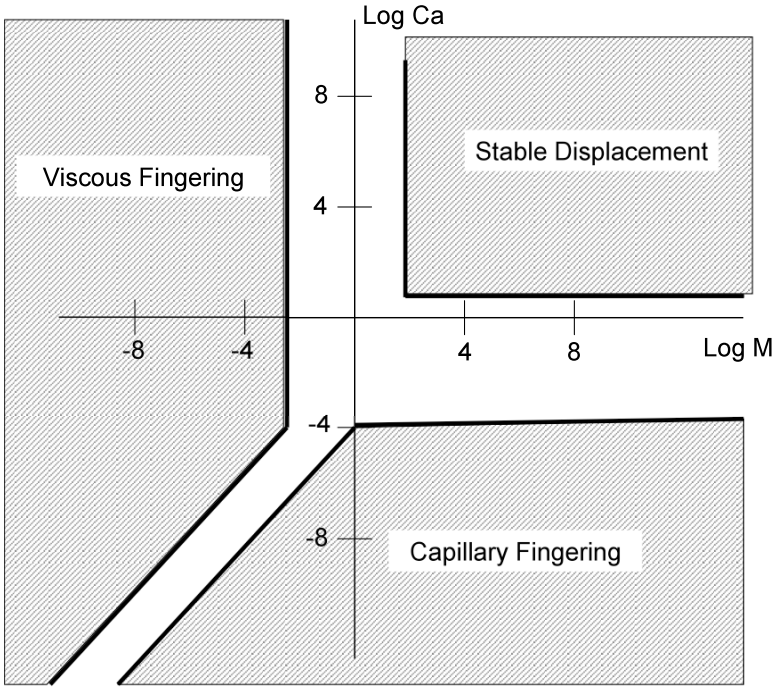

Figure 20. Lenormand diagram (after Lenormand et al, 1988).

The diagram shows the existence of three basic domains for fluid penetration: stable displacement, viscous fingering, and capillary fingering. In the stable displacement region, the major force is due to viscosity interaction of the injected fluid. The flow shows a flat front moving towards the exit with some irregularities with the dimensions of a few pore scales. In the viscous fingering region the major force is due to viscosity interaction of the displaced fluid. In this type of flow, the fingers look like a tree with no loops and they spread across the porous network growing towards the exit. In the capillary fingering region, the major force is due to capillarity, which also exhibits tree-like fingering, but the fingers grow in all directions, even toward the entrance forming loops. These loops trap the displaced wetting fluid, leading to a higher final saturation than the viscous fingering.

Figure 21 shows 2D simulations of the interface advance using the He-Chen-Zhang model applied to a packed bed of sand particles where the pore network structure has been captured by XMT analysis. In this simulation, a 2D XMT image slice has been used and flow goes from top to bottom, induced by a fixed pressure difference. Simulation parameters are set in such a way as to obtain flow in the transition zone between capillary fingering and stable displacement as described by Lenormand. The capillary number (Ca) is 6.77×10^{-2} and the density ratio of 3.

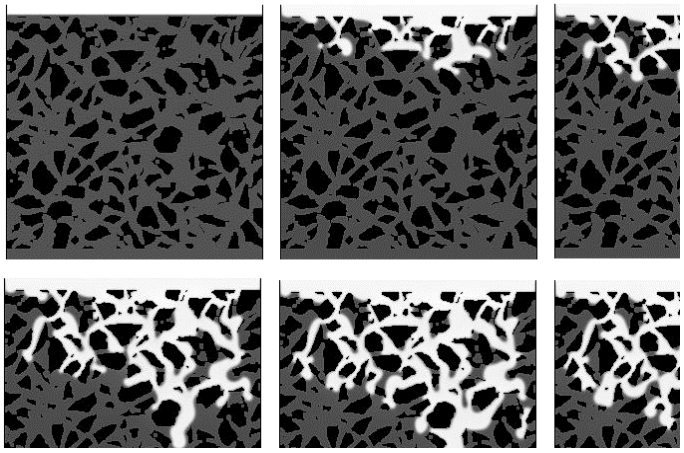

Figure 21. Sequence of simulations of two-phase flow in a packed bed of sand particles. Percolation simulations by the single component He-Chan-Zhang LBM with $\rho_l / \rho_g = 3.0$ and Ca = 6.77×10^{-2}. Lattice size of 256x256. Images shown after each 5000 iteration steps.

As can be seen in the sequence of images, the simulation starts from complete saturation of the wetting phase that is subsequently displaced by a non-wetting phase (white). In the course of the simulation, the flow goes through the less resistant paths (coarser pore diameters), leaving behind some residual wetting phase trapped in very small pore spaces with high flow resistance where the non-wetting phase cannot enter until the pressure increases. In agreement with the diagram proposed by Lenormand et al (1988), even though we are working at a pore scale level, the pattern of percolation shows a capillary fingering type of flow with relatively short fingers.

Figure 22 shows a comparison of the same structure shown in Figure 21 with a 2D simulation condition where the surface tension is varied. Comparison at the same level of iteration shows that the percolation follows the same pattern for both simulations in this porous network structure, probably due to the fact that

both simulations are run with the same pressure gradient and therefore the path of least resistance has not changed. However, reduction of the surface tension produces longer and thinner fingers.

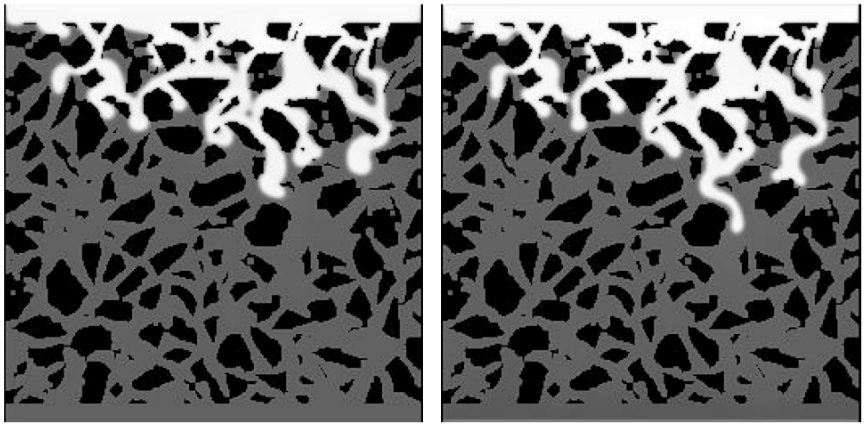

Figure 22. Two penetration simulations with different surface tensions ($\bar{k}$) but the same $\rho_l / \rho_g = 3.0$ and pressure gradient. Left: high surface tension ($\bar{k}$=0.1, Ca = 6.77x10-2). Right: low surface tension ($\bar{k}$=10^{-5}, Ca = 230). Both images after 10000 iterations.

Figure 23 shows a comparison between the 2D simulations of Figure 21 (left image) with a simulation where the density ratio has been inverted (right image). In this new case, the low density fluid displaces the heavier fluid and the pattern of flow changes since the pressure field has changed. According to the Lenormand diagram (Figure 20), a stronger viscous fingering type of flow is expected with more and longer fingers being formed due to the stronger viscous interaction and interface front instability. There is a clear qualitative agreement between theory and simulations. Fingers are formed in zones of low resistance to flow. Once formed, they start growing rapidly toward the exit.

The He-Chen-Zhang model has advantages over other methods such as its thermodynamic consistency, which makes the treatment of the surface tension easier because it can be set before actually running the simulation. On the other hand, it has not been extended to consider more than one component, so two-phase flow is a mathematical artifact where both fluid phases are related by an equation of state. This characteristic imposes some restrictions; under certain pressure changes and flow conditions, unexpected condensation and evaporation of the phases can be induced.

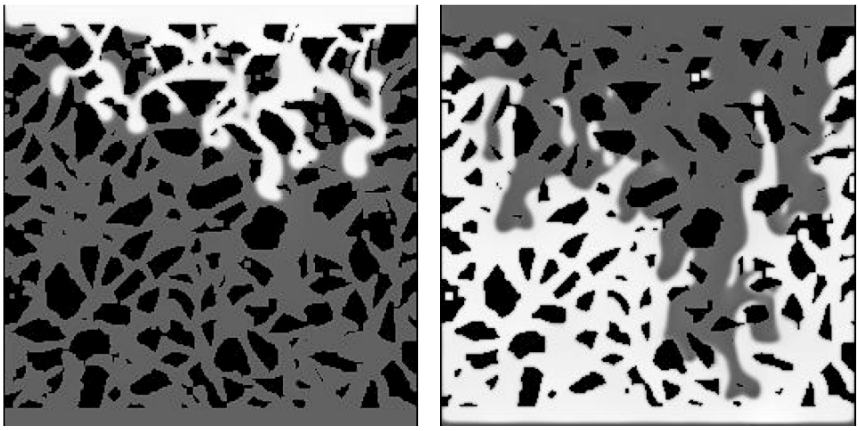

Figure 23. Two different penetration simulations for the same surface tension but inverse density ratio. Left: density ratio =3/1 and Ca = 6.77×10^{-2}. Right: density ratio =1/3 and Ca = 1.32×10^{-1}. Both images after 10,000 iterations.

Although the use of an equation of state to induce phase segregation is a simple and elegant formulation for interfacial dynamics simulation, it restricts the one component simulation to industrial applications such as liquid-vapor phase systems (e.g. water/water-vapor). Nevertheless, the simulations provide a better understanding of complex, multiphase problems if we use the concept of dynamic similitude for fluid flow conditions and if the condensation/evaporation effect can be assumed to be negligible.

Application of single component multiphase flow LBM (He-Chen-Zhang model) coupled with XMT analysis to define the complex pore geometry allows for simulation of flow in porous media. The model is used for simulation of fluid penetration into porous samples and the analysis of capillary phenomena. At present, the LBM has been applied to 3D simulations of fluid penetration into oil sand samples digitalized by XMT. Results from LBM simulations of multiphase flow through oil sand systems are shown in Figures 24 and 25 for oil sands from Athabasca and Sunnyside, respectively. A more uniform pore network structure and a stable displacement was observed due to the narrow size distribution of the sands from the Athabasca oil sands sample. For the Sunnyside oil sand sample, a complex pore network structure and capillary fingering was observed due to the widespread size distribution of the sands.

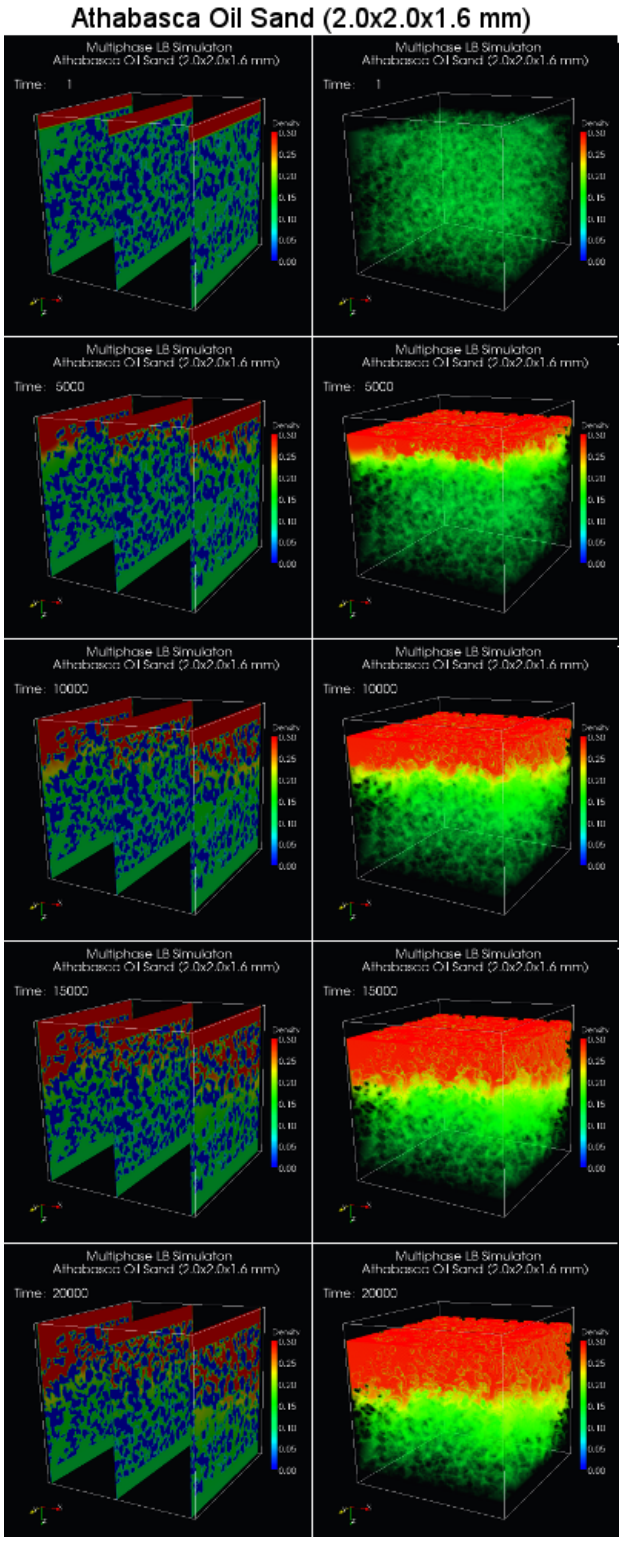

Figure 24. Results of LB simulation of multiphase flow through Athabasca oil sand sample. Images top to bottom show flow after 1, 5000, 10000, 15000 and 20000 iterations.

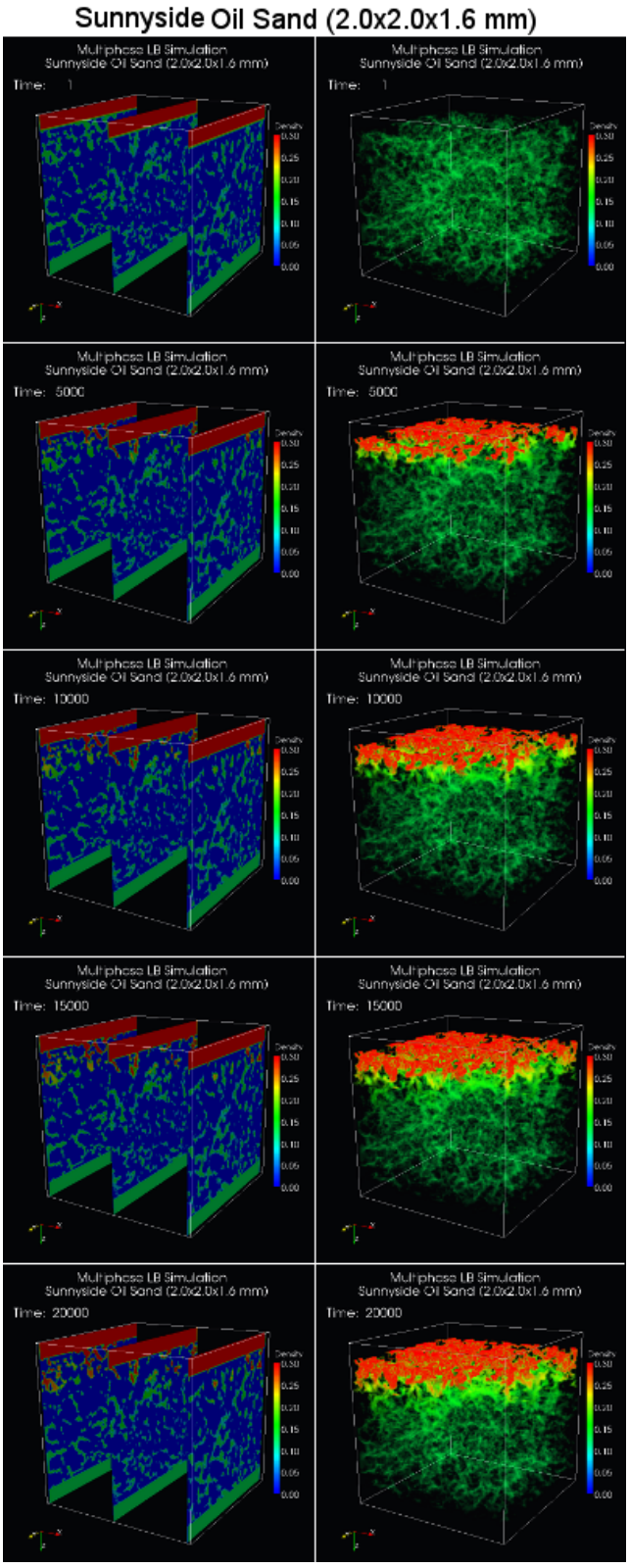

Figure 25. Results of LB simulation of multiphase flow through Sunnyside oil sand sample. Images top to bottom show flow after 1, 5000, 10000, 15000 and 20000 iterations.

4 Conclusions and Recommendations

Detailed 3D imaging of oil shale cores using multiscale X-ray CT was done before and after pyrolysis to establish the pore structure of the core after reaction. The pore structure of the unreacted material was not clear. Selected images of a core pyrolyzed at 400°C were obtained at a voxel resolution from 39 μm to 60 nm. It was evident that XNT imaging is required for satisfactory pore structure information for the silicate-rich zone. Some of the pore space created during pyrolysis was clearly visible at this resolution and it was possible to distinguish between the reaction products and the host shale rock.

In addition, scanning of oil shale core samples after pyrolysis at three reaction temperatures (300°C, 350°C, and 400°C) and heating rates of 1, 10 and 100°C/min was done to establish the pore structure of the core after reaction using HRXMT for imaging (~ 5 micron voxel resolution). The porosity variation with drill core sample height as measured from the CT data clearly correlated with position of the kerogen layers. The mean porosity of the silicate-rich layers inside the reacted core was found to be about 10% for the heating rates of 1 and 100°C/min. For a heating rate of 10°C/min, the mean porosity of the silicate-rich layers inside the reacted core was about 20%, a difference attributable to a thermocouple drill hole for the sample. It should be noted that the reported porosity may be overestimated since residual kerogen and kerogen reaction products may be included. Additional CT analysis is warranted.

The pore structure deduced from the images was used for LB simulations to calculate the permeability in the pore space. The permeabilities of the silicate-rich zone of the pyrolyzed samples were on the order of millidarcies, while the reacted core permeabilities of the kerogen-rich zone were very anisotropic and about four orders of magnitude higher. Further, we have been successful in implementing the 2D and 3D software capabilities of the LB simulation code for analysis of multiphase fluid flow in porous media. Software implementation includes:

1. LB codes have been parallelized due to the computational demand. Several processors can be used to make the memory requirements affordable and the time of simulation practical for this complex multiphase flow problem,
2. Verification of the code with the analytical solution of Laplace's law has been done to establish agreement with the surface tension model necessary to describe wetting and capillary filling of small pores,
3. Verification of the interaction between solid and fluid phases was done with the analytical solution for pipe flow of two fluids of different viscosity/density.

The single component multiphase flow He-Chen-Zhang LBM model has been extended to incorporate fluid-solid interaction forces and has been applied to the simulation of percolation with actual XMT images of pore network structures for the Athabasca and Sunnyside oil sand samples.

Research on pore scale transport processes in the pyrolysis of oil sand and oil shale involves multiscale, 3D X-ray CT analysis coupled with LB simulation. Future research will identify critical fundamental factors of pore geometry and structure which limit recovery of hydrocarbons from oil sand and oil shale. The next phase of research includes:

- Analysis of new, fresh oil shale core and comparison with the initial oil shale samples
- Calibration for phase identification with results from QEM/SCAN.
- Directional (anisotropic) permeability of the reacted core of new oil shale samples for pyrolysis reactions at different temperatures based on pore network structure by XMT analysis coupled with LB simulation.
- Permeability of the reacted core after pyrolysis reactions under different loading conditions.

5 List of publications/presentations

1. "Advanced 3D Multiphase Flow Simulation in Porous Media Reconstructed from X-ray Micro Tomography Using the He-Chen-Zhang Lattice Boltzmann Model" by C.L. Lin, A.R. Videla and J.D. Miller, *Flow Measurement and Instrumentation*, 21 (2010) 255-261.
2. Poster presentation by C.H. (Ken) Hsieh, ICSE graduate student, "Pore Scale Analysis of Oil Sand/Oil Shale Pyrolysis by X-ray micro CT and LB Simulation" , C.L. Lin, J.D. Miller, and C.H. Hsieh, ICSE Meeting (Unconventional Fuels Conference) U of U, 28 April, 2010.
3. "Pore Scale Analysis of Oil Shale Pyrolysis by X-ray CT and LB Simulation" , C.L. Lin, J.D. Miller, C.H. Hsieh, P. Tiwari and M.D. Deo, Submitted for publication in the Proceeding of 6th World Congress on Industrial Process Tomography, Beijing, China, Sep. 2010.
4. "Flow Simulation with the Lattice Boltzmann Method in 3D Porous Structures of Pyrolyzed Oil Shale Cores using Multiscale X-ray CT Imaging", C.L. Lin, J.D. Miller, C.H. Hsieh, presented at 2010 AICHE conference, Salt Lake City Utah, Nov. 2010.

6 References

Chen, H. (1993). Discrete Boltzmann systems and fluid flow*s, Comput. Phys*, 7 632-637.

Chen, S. and Doolen G. (1998). Lattice Boltzmann method for fluid flows, *Annu. Rev. Fluid. Mech.*, 30 329-364.

He, X., Shan, X., and Doolen, G. (1998). Discrete Boltzmann equation model for nonideal gases, *Phys. Rev. E*, Vol 57, pp R13-R16.

He, X., Chen, S., and Zhang, R. (1999). A lattice Boltzmann scheme for incompressible multiphase flow and its applications in simulation of Rayleigh-Taylor instability, *J. Comput. Phys.*, 152 642-663.

He, X. and Doolen, G. (2002) Thermodynamics foundations of kinetic theory and lattice Boltzmann models for multiphase flow, *J. Stat. Phys.*, 107 309-328.

He, X. and Luo L.-S. (1997), Theory of the lattice Boltzmann method: From the Boltzmann equation to the lattice Boltzmann equation, *Phys Rev E*, 56 6811-6817.

Kang, Q., Zhang, D., and Chen, S. (2004). Immiscible displacement in a channel: simulations of fingering in two dimensions, *Advances in Water Resources*, 27 13-22.

Lenormand, R, Touboul E, and Zarcone, C., (1988). Numerical methods and experiments on immiscible displacements in porous media, *J. Fluid Mech*. 189:165-87.

Lin, C.L. and Miller, J.D. (2004). Pore structure of particles beds for fluid transport simulation during filtration, *Int J Miner Process*, 73 281-294.

Marle, C.M., (1981). *Multiphase Flow in Porous Media*, Houston: Gulf Publishing Company.

Martys, N. and Chen, H. (1996). Simulation of multicomponent fluids in complex three-dimensional geometries by the Lattice Boltzamnn model, *Phys. Rev. E,* 53 743-750.

Miller, J.D. and Lin, C.L. (2004). Three-dimensional analysis of particulates in mineral processing systems by cone-beam x-ray microtomography. *Minerals and Metallurgical Processing*, 21(3) 113-124.

Qian. Y., d'Humieres D. and Lallemand, P. (1992). Lattice BGK models for Navier-Stokes equation, *Europhys. Lett.*, 17 479-484.

Rothman, D.H., and Zaleski, S. (1991). Lattice-gas models of phase separation: interfaces, phase transitions, and multiphase flow, *Rev. Mod. Phys*. 6:1417.

Shan, X. and Chen, H. (1993). Lattice Boltzmann model for simulating flows with multiple phases and components*, Phys. Rev. E*, 47 1815-1819.

Stockman, H. (1999). A 3D Lattice Boltzmann code for modelling flow and multi-component dispersion, Sandia National Laboratories, SAND99-0162.

Succi, S., (2001). The Lattice Boltzmann equation for fluid dynamics and beyond, Oxford University Press, New York.

Sukop, M.C. and Or, D. (2003). Invasion percolation of single component, multiphase fluids with lattice Boltzmann models, Phys B, 338 298-303.

Swift, M.R., Osborn, W.R., and Yeomans, J.M. (1995). Lattice Boltzmann simulation of nonideal fluids, *Phys. Rev. Lett.*, Vol. 75, pp 830-833.

Swift, M.R., Orlandini, E., Osborn, W.R., and Yeomans, J.M. (1996). Lattice Boltzmann simulations of liquid-gas and binary fluid systems, *Phys. Rev. E*, Vol. 54, pp 5041-5052.

Videla, A.R., Lin C.L., and Miller, J.D. (2008). Simulation of saturated fluid flow in packed particle beds – the Lattice-Boltzmann method for the calculation of permeability from XMT images, *Journal of Chinese institute of Chemical engineers*, 9 117-128.

Videla, A.R., 2009. Explorations in three-dimensional Lattice Boltzmann simulation for fluid flow in packed particle bed. Ph. D. Dissertation, University of Utah.

Wolf-Gladrow, D. (2000). Lattice-Gas Cellular Automata and Lattice Boltzmann Models, Springer, New York.

XRADIA, 2010, http://www.xradia.com.

Zhang, R., He, X., and Chen, H. (2000). Interface and surface tension in incompressible Lattice Boltzmann multiphase model. *Comput Phys Comm*. 129:121.

National Energy Technology Laboratory

626 Cochrans Mill Road
P.O. Box 10940
Pittsburgh, PA 15236-0940

3610 Collins Ferry Road
P.O. Box 880
Morgantown, WV 26507-0880

13131 Dairy Ashford, Suite 225
Sugarland, TX 77478

1450 Queen Avenue SW
Albany, OR 97321-2198

2175 University Ave. South
Suite 201
Fairbanks, AK 99709

Visit the NETL website at:
www.netl.doe.gov

Customer Service:
1-800-553-7681